Microstructural and magnetotransport properties of $La_{0.7}Ca_{0.3}MnO_3/BaTiO_3$ and $La_{0.7}Sr_{0.3}MnO_3/BaTiO_3$ bilayered films

Y. P. Lee,* S. Y. Park, Y. H. Hyun, and J. B. Kim

q-Psi and Department of Physics, Hanyang University, Seoul, 133-791 Korea

V. G. Prokhorov and V. A. Komashko

Institute of Metal Physics, NASU, Kiev, 03142 Ukraine

V. L. Svetchnikov

National Center for HREM, TU Delft, 2628AL, The Netherlands

The microstructural and the magnetotransport properties of $La_{0.7}Ca_{0.3}MnO_3$ and $La_{0.7}Sr_{0.3}MnO_3$ films, deposited on a $BaTiO_3$ layer (LCMO/BTO and LSMO/BTO, respectively), and on $LaAlO_3$ and $SrTiO_3$ (001) single crystals (LCMO/LAO, LSMO/LAO and LSMO/STO) by rf-magnetron sputtering using the "soft" (or powder) targets, have been investigated. The films grown on BTO demonstrate biaxial tensile in-plane and compressive out-of-plane strains, while those grown on LAO show the opposite trend, i.e., compressive in-plane and tensile out-of-plane strains. The films with a biaxial tensile in-plane strain undergo the magnetic transition at a higher temperature than those with a biaxial compressive one. This implies that the variation of Mn-O-Mn bond angle, controlled by the lattice strain, plays a more important role in the formation of spin ordering in the manganite film than the modification in the Mn-O bond length does. It was shown that the magnetic inhomogeneity, observed through the difference between field-cooled and zero-field-cooled temperature-dependent magnetization, is not greatly relevant to the electronic nature, but is controlled by the lattice distortion and the microstructural defects. The observed enhancement of magnetoresistance for the LSMO/BTO bilayer at room temperature makes this material system promising in the development of new hybrid ferromagnetic/ferroelectric devices.

I. INTRODUCTION

The discovery of colossal magnetoresistance (CMR) in doped manganite perovskites[1] with the general formula $R_{1-x}A_xMnO_3$, where R is a rare-earth cation and A is alkali or alkaline earth cation,[2,3] stimulated numerous investigations because of not only their interesting fundamental science but also their possibility for device applications. For the potential industrial applications, these materials should be prepared in the form of thin films or multilayered hybrid systems. However, thin manganite films frequently exhibit different magnetotransport properties from those of the bulk materials. The observed discrepancy is mainly explained by the lattice strain, due to the epitaxial growth of the film, which greatly affects the formation of the spin-ordered state and the value of the CMR effect.[4–12] It was argued that, for example, a lattice compression would reduce the electron-phonon interaction and increase the electronic hopping probability by decreasing the Mn-O bond length and increasing the Mn-O-Mn bond angle, all leading to an increase of the Curie temperature (T_C). In contrast, the Jahn-Teller distortion induces a localization of electrons and reduces T_C.[4] This phenomenon can be described basically by the Millis model,[13] developed for materials with a weak lattice strain and a cubic symmetry. On the other hand, the recently observed suppression of a contribution from the Jahn-Teller distortion to the ferromagnetic ordering, with increasing the lattice mismatch between substrate and film,[7,12,14,15] manifests a physical limit of the weak-strain approach[13] in describing the magnetic properties of manganite films. Moreover, it was shown that the microstructure features[9,15,16] and the oxygen content[6,17–22] could lead to considerable changes in the magnetotransport properties of films, as well. Although the influence of single-crystalline substrates on the magnetic and the electronic properties of manganite films has been extensively investigated, the development of hybrid devices such as ferromagnetic/ferroelectric ones, which are very promising for modern applications,[23] needs more detailed information on the microstructure of interfaces and the mutual influence between adjacent layers.

In this paper, we report our experimental results for ferromagnetic/ferroelectric hybrid films of $La_{0.7}Ca_{0.3}MnO_3$ and $La_{0.7}Sr_{0.3}MnO_3$, deposited on a $BaTiO_3$ layer (LCMO/BTO and LSMO/BTO). For comparison, we also present the same data for the films deposited on bare $LaAlO_3$ (001) and $SrTiO_3$ single-crystalline substrates LCMO/LAO and LSMO/LAO, and LCMO/STO and LSMO/STO, respectively. The observed difference in growth mechanism of the LCMO and the LSMO films, and the effects of lattice strain and microstructure peculiarities on the magnetotransport properties will be discussed in detail.

II. EXPERIMENTAL TECHNIQUES

Several different films were prepared by on-axis rf-magnetron sputtering using the so-called "soft" (or powder) target.[24] The substrate was a LAO(001) single crystal with an out-of-plane lattice parameter of $c \simeq 0.379$ nm for the
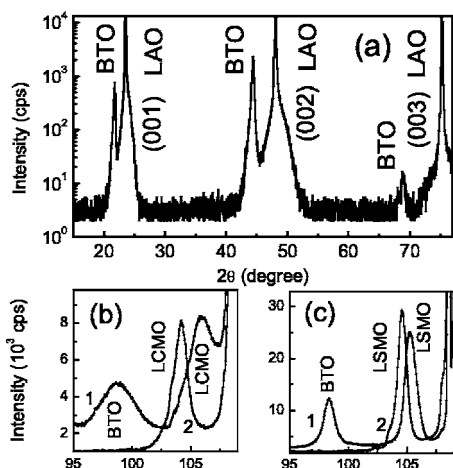
FIG. 1. (a) θ-2θ XRD pattern of the BTO/LAO system. (004) Bragg peaks for (b) the LCMO and (c) the LSMO films, deposited on BTO (1) and LAO (2).
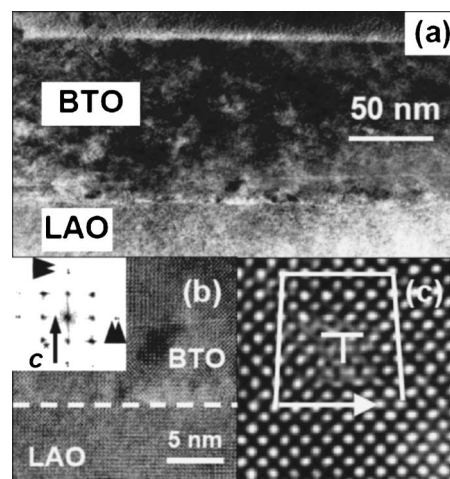

FIG. 2. (a) Low-magnification cross-sectional HREM image for the BTO/LAO system. (b) High-magnification cross-sectional HREM image for the BTO/LAO interface. The dashed line indicates the interface. Inset: FFT. (c) Misfit dislocation formed in the BTO film near the interface. The associated Burger's circuit is indicated as a white line.

pseudocubic symmetry. The total pressure in the chamber was 4×10^{-2} Torr with a gas mixture of Ar and O_2 (2:1). The substrate temperature during deposition was 750 $^{\circ}$C. The LCMO/BTO and the LSMO/BTO bilayers were prepared with thicknesses for LCMO, LSMO, and BTO of $d \simeq 160$, 160, and 100 nm, respectively. For comparison, the bare BTO, the LCMO, and the LSMO films with the same thicknesses were also deposited on the LAO substrate under similar conditions. The LSMO films on STO had a thickness of $d \simeq 70$ nm. The θ-2θ x-ray diffraction (XRD) patterns were obtained using a Rigaku diffractometer with Cu K_{α} radiation. The high-resolution electron-microscopy (HREM) studies were carried out by using a Philips CM300UT-FEG microscope with a field emission gun operated at 300 kV. The point resolution of the microscope was in the order of 0.12 nm. The cross-sectional specimens were prepared by the standard techniques using mechanical polishing followed by ion-beam milling at a grazing incidence. All microstructure studies were carried out at room temperature. The resistance measurements were performed by using the four-probe method in the temperature range of 4.2–300 K under a magnetic field up to 5 T. The in-plane field-cooled (FC) and the zero-field-cooled (ZFC) magnetization curves under an applied magnetic field of 100 Oe and the magnetization hysteresis loops at 10 K were taken with a Quantum Design superconducting quantum interference device magnetometer.

III. MICROSTRUCTURES OF THE FILMS

Figure 1(a) shows the θ-2θ XRD scan for the BTO film deposited on the LAO substrate. The high intensity of the (00l) peaks manifests that the deposition results in highly c-oriented films. The obtained out-of-plane lattice parameter ($c \simeq 0.407$ nm) is not very different from the bulk value at room temperature $c \simeq 0.4033$ nm.[25] Figures 1(b) and 1(c) display the (004) Bragg peaks in detail for the LCMO/BTO and the LCMO/LAO, and the LSMO/BTO and the LSMO/LAO films, respectively. The analysis of XRD data reveals that the out-of-plane lattice parameter for LCMO/LAO cor-

responds to $c \simeq 0.3900$ nm, while $c \simeq 0.3857$ nm for LCMO/BTO. Similar, $c \simeq 0.3891$ nm for LSMO/LAO, while $c \simeq 0.3872$ nm for LSMO/BTO.

Figure 2 presents (a) the low-magnification cross-sectional HREM image of the BTO film and (b) a high-magnification image of the interface with fast Fourier transformation (FFT) as inset. The FFT image across the BTO/LAO interface reveals elongated and slightly split spots in both c (normal to the interface) and a (parallel to the interface) directions (indicated by black arrows). This is an evidence for semicoherent (or weakly coherent) lattice coupling between LAO and BTO. Due to the large mismatch between substrate and film, the misfit dislocations are formed in the BTO near the interface, as displayed in Fig. 2(c). An associated Buerger's circuit is indicated by the white line. The measurement of various interspot spacings on the high-magnification HREM image allows us to obtain the average values of lattice parameters. Analysis reveals that the BTO film has a tetragonal crystal lattice with $c \simeq 0.407$ nm and $c/a \simeq 1.020$. The obtained lattice parameters are in good agreement with those for the bulk[25] and for BTO films deposited on SrTiO$_3$ ($a \simeq 0.391$ nm).[26] A slightly enhanced tetragonal ratio in our case can be explained by larger in-plane compressive lattice strain in the film deposited on the substrate with a smaller lattice constant.

Figure 3 presents the low-magnification cross-sectional HREM image of (a) the LCMO/BTO bilayer, (b) the high-magnification one, and (c) the FFT pattern for the interface. It is seen that FFT of the LCMO/BTO interface produces a rectangular pattern of the spots, which are elongated only along the out-of-plane direction without a visible splitting or an elongation along the in-plane one. This indicates that an almost coherent interface is formed between BTO and LCMO. The analysis of interspot spacing, and angles between the rows and the columns reveals that the LCMO layer has a tetragonal crystal structure with $c \simeq 0.386$ nm, which is
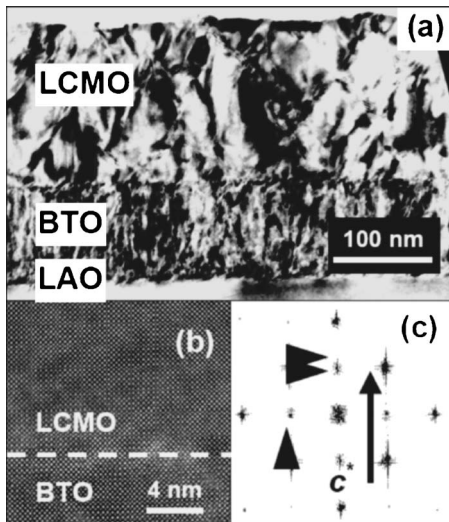
FIG. 3. (a) Low-magnification cross-sectional HREM image for the LCMO/BTO film. (b) High-magnification cross-sectional HREM image of the LCMO/BTO interface. The dashed line indicates the interface. (c) FFT of the HREM image in (b).

in good coincidence with the XRD data, and has a reversed (with respect to BTO) tetragonal ratio, $c/a \simeq 0.980$. The estimated in-plane lattice parameter for LCMO, $a \simeq 0.394$ nm, turns out to be very close to that for BTO, $a \simeq 0.399$ nm.

For comparison a similar microstructural analysis has also been carried out for a LCMO film deposited directly on LAO. As displayed in Fig. 4, the FFT image of this case produces a rectangular pattern similar to that for the LCMO/BTO interface, with well-defined spots split along the out-of-plane direction and slightly elongated spots along the in-plane one, manifesting a nearly coherent interface between the film and the substrate. The LCMO/LAO film reveals a tetragonal structure with $c \simeq 0.390$ nm, which is perfectly co-incident with the corresponding XRD data, and $c/a \simeq 1.015$.

The same cross-sectional HREM images for LSMO/BTO and LSMO/LAO are displayed in Figs. 5 and 6, respectively. For both films the FFT images exhibit slightly elongated

FIG. 5. (a) Low-magnification cross-sectional HREM image for the LSMO/BTO film. (b) High-magnification cross-sectional HREM image of the LSMO/BTO interface. The dashed line indicates the interface. Inset shows moire pattern across the interface with misfit dislocations (indicated by white arrows). (c) FFT of the HREM image in (b).

spots along the in-plane and out-of-plane directions, where this effect is slightly larger for the LSMO/LAO film. The analysis of the high-magnification images reveals that the tetragonal distortion of the LSMO layers is significantly smaller than that for LCMO ones: $c/a \simeq 0.996$ for LSMO/BTO and $c/a \simeq 1.008$ for LSMO/LAO. Insets in Figs. 5(b) and 6(b) display moire patterns (inverse Fourier transforms[27]) of the high-magnification HREM images across the interfaces of LSMO/BTO and LSMO/LAO, respectively. It is seen that in both cases misfit-edge disloca-
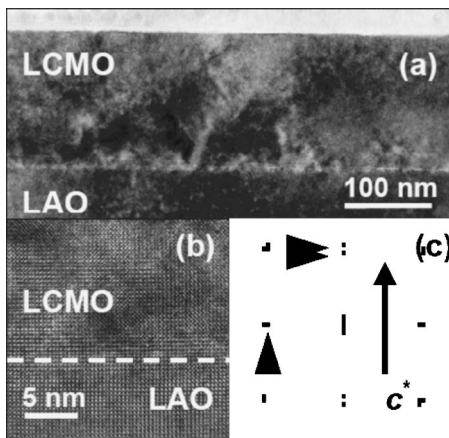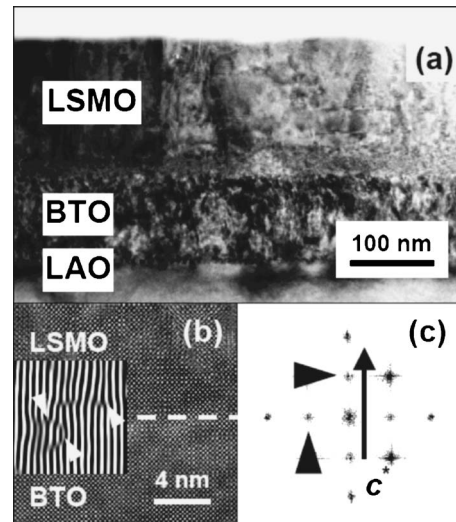

FIG. 4. (a) Low-magnification cross-sectional HREM image for the LCMO/LAO system. (b) High-magnification cross-sectional HREM image of the LCMO/LAO interface. The dashed line indicates the interface. (c) FFT of the HREM image in (b).
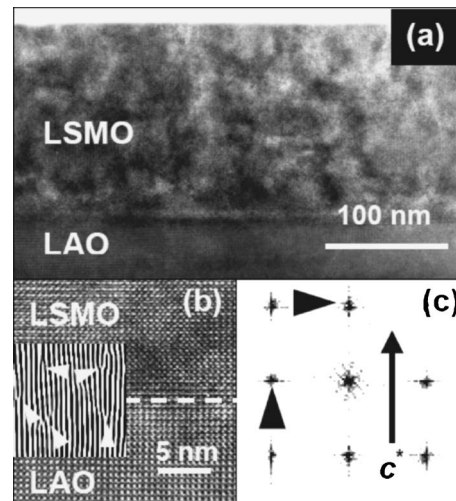

FIG. 6. (a) Low-magnification cross-sectional HREM image for the LSMO/LAO system. (b) High-magnification cross-sectional HREM image of the LSMO/LAO interface. The dashed line indicates the interface. Inset shows moire pattern across the interface with misfit dislocations (indicated by white arrows). (c) FFT of the HREM image in (b).

TABLE I. Results of the XRD and the HREM analysis for the investigated films.

Samples	Out-of-plane lattice parameter c (nm), XRD data	Tetragonal ratio c/a, HREM data	In-plane strain ϵ_{100} (%)	Out-of-plane strain ϵ_{001} (%)	Bulk strain ϵ_B (%)[a]	Jahn-Teller strain ϵ_{JT} (%)[b]
BTO/LAO	0.407	1.02	0.12	−0.92	−0.68	−0.84
LCMO/BTO	0.3857	0.99	−0.93	0.46	−1.4	1.14
LCMO/LAO	0.39	1.015	0.57	−0.64	0.49	−1.0
LSMO/BTO	0.3872	0.996	−0.36	0.53	−0.2	0.73
LSMO/LAO	0.3891	1.008	0.6	−0.19	1.01	−0.65
LSMO/STO	0.3869	0.993	−0.1	0.6	0.41	0.57
LSMO/BTO[c]	0.3864	0.98	−1.29	0.73	−1.86	1.66
LSMO/LAO[c]	0.3903	1.01	0.72	−0.27	1.17	−0.81

[a]$\epsilon_B = (2\epsilon_{100} + \epsilon_{001})$.
[b]$\epsilon_{JT} = \sqrt{2/3}(\epsilon_{001} - \epsilon_{100})$.
[c]The thickness of LSMO layer is $d \simeq 70$ nm.

tions are formed in the LSMO film (noted by white arrows). Moreover, these dislocations can be in opposite directions. Therefore, one can conclude that the semicoherent interface between the substrate and the film is formed during the deposition of LSMO.

The lattice parameters and the estimated values of in-plane [$\epsilon_{100} = (a_{bulk} - a_{film})/a_{bulk}$] and out-of-plane [$\epsilon_{001} = (c_{bulk} - c_{film})/c_{bulk}$] lattice strains for investigated samples are summarized in Table I. Table I also includes the data for the LSMO/STO thin films with $d \simeq 160$ nm and for the LSMO/BTO and the LSMO/LAO thin films with $d \simeq 70$ nm, for the comparison. The following bulk lattice parameters are employed in this evaluation: $a_{bulk} \simeq 0.3864$ nm and $c_{bulk} \simeq 0.3875$ nm for La$_{0.7}$Ca$_{0.3}$MnO$_3$ (Ref. 28) and $a_R^{bulk} \simeq 0.5480$ nm and $\alpha_R^{bulk} \simeq 60.3°$ for La$_{0.7}$Sr$_{0.3}$MnO$_3$.[29] Here, the subscript "R" stands for rhombohedral.

Therefore, two kinds of films with different signs of lattice strain have been prepared: LCMO/BTO and LSMO/BTO have biaxial tensile in-plane and compressive out-of-plane strains while the LCMO/LAO and LSMO/LAO films are exposed reversely to compressive in-plane and tensile out-of-plane strains. On the other hand, it is seen that the LCMO films are more susceptible to the crystal structure of the substrate and the lattice strains are accumulated more than the LSMO ones during deposition. The observed difference in the lattice-strained state for these films can be governed by the peculiarities of the growth mechanism. Recently, it has been shown that the LSMO films tend to stress relaxation during the growth by the formation of misfit dislocations while the LCMO ones form a columnlike strained microstructure.[30–32] These results absolutely agree with ours, testifying that the LCMO films demonstrate a dislocation-free epitaxial-growth mode with the formation of a strong lattice-strained state. These biaxial strains are accommodated, during the film growth, by forming a coherent columnar microstructure directed normal to the interface, which can be treated as prismatic antiphase boundaries. However, in the LSMO films the strain accommodation is realized by the misfit-dislocation formation.

IV. EXPERIMENTAL RESULTS OF THE TRANSPORT AND THE MAGNETIC PROPERTIES

Figure 7 shows the in-plane FC and ZFC temperature-dependent magnetization curves, $M(T)$, for (1) the LCMO/BTO and (2) the LCMO/LAO systems. The applied magnetic field was $H = 100$ Oe. The LCMO/BTO bilayer manifests the onset of the ferromagnetic ordering at $T_C \simeq 250$ K while LCMO/LAO has T_C at a lower temperature, $T_C \simeq 230$ K, which is typical for the lattice-strained as-deposited film.[9,10,12,33] The inset of Fig. 7 displays the in-plane hysteresis loops, measured at $T = 10$ K, for the LCMO/BTO and the LCMO/LAO films. The LCMO/BTO film has narrower $M(H)$ curve than LCMO/LAO (the coercive field, $H_c \simeq 100$ and 300 Oe, respectively) and saturates (saturation field, $H_s \simeq 3000$ Oe) twice as fast as LCMO/LAO ($H_s \simeq 6000$ Oe). This can be explained by a strain-driven magnetic anisotropy in these films.[5,34]
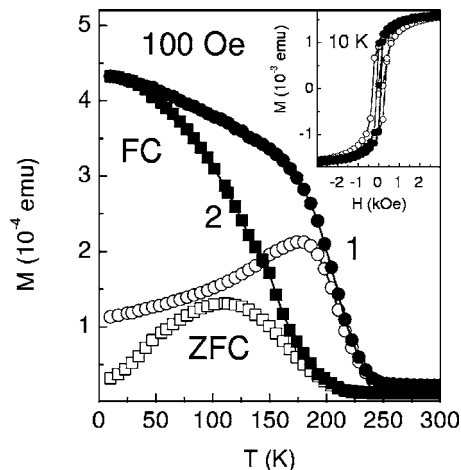

FIG. 7. Temperature dependence of the FC (solid symbols) and the ZFC (open symbols) magnetizations for LCMO/BTO (1) and LCMO/LAO (2). The inset displays the in-plane magnetic hysteresis loops for LCMO/BTO (solid symbols) and LCMO/LAO (open symbols) at 10 K. Lines guide the eye.
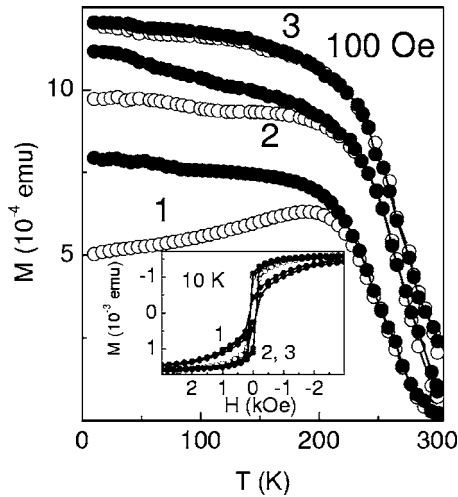
FIG. 8. Temperature dependence of the FC (solid symbols) and the ZFC (open symbols) magnetizations for LSMO/LAO (1), LSMO/BTO (2), and LSMO/STO (3). The inset displays the in-plane magnetic hysteresis loops at 10 K. Lines guide the eye.

Figure 8 displays the same magnetization dependencies for (1) the LSMO/LAO, (2) the LSMO/BTO, and (3) the LSMO/STO films. The maximal temperature of the ferromagnetic ordering is observed for LSMO/STO, $T_C \simeq 315$ K, while the lowest one belongs to LSMO/LAO, $T_C \simeq 296$ K. The LSMO/BTO film has $T_C \simeq 310$ K. The inset in Fig. 8 shows that the coercive field is the same for all LSMO films, $H_c \simeq 100$ Oe, while the saturation one is considerably dependent on the substrate: $H_s \simeq 4000$, 1200, and 800 Oe for LSMO/LAO, LSMO/STO, and LSMO/BTO, respectively.

Figure 9 is the temperature-dependent resistance $R(T)$ for (1) the LCMO/BTO and (2) the LCMO/LAO films with and without an applied magnetic field of 5 T. The magnetic field was directed parallel to the film surface and perpendicular to the transport current. It is seen that the LCMO/BTO bilayer
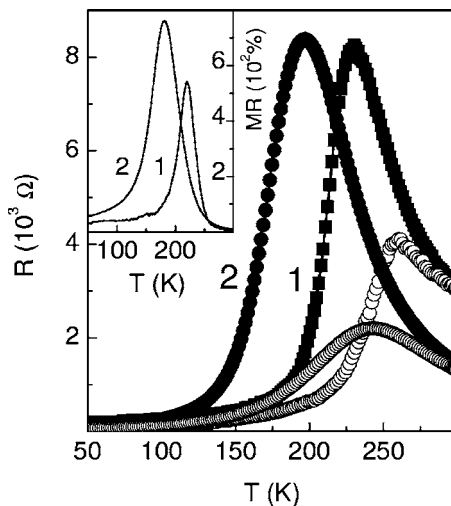

FIG. 9. Temperature dependence of the resistance for LCMO/BTO (1) and LCMO/LAO (2) without (solid symbols) and with (open symbols) an applied magnetic field of 5 T. The inset includes the temperature-dependent MR ratios. Lines guide the eye only.
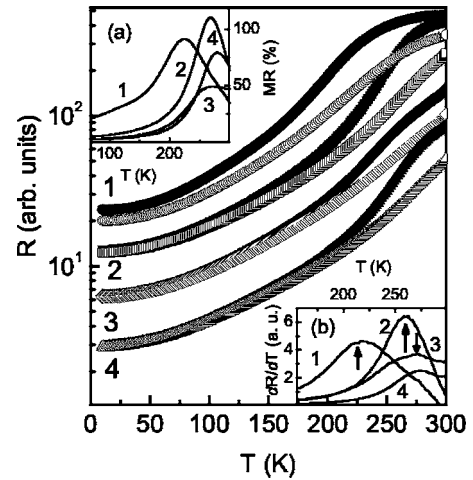

FIG. 10. Temperature dependence of the resistance for LSMO/LAO (1) and LSMO/BTO (2) with $d=70$ nm, and LSMO/LAO (3) and LSMO/BTO (4) with $d=160$ nm without (solid symbols) and with (open symbols) an applied magnetic field of 5 T. Inset (a) includes the temperature-dependent MR ratios. Inset (b) displays the temperature-dependent first derivative dR/dT. The MI transition temperatures are indicated by arrows.

undergoes the metal-insulator (MI) transition at $T_P \simeq 230$ K while the LCMO/LAO film manifests $T_P \simeq 195$ K. In both cases the temperature of MI transition is lower than the corresponding T_C, and this can be understood by a percolating nature of the MI transition.[35] The inset of Fig. 9 presents the temperature dependence of negative magnetoresistance (MR) for (1) LCMO/BTO and (2) LCMO/LAO. The MR value is defined by $100\% \times [R(0)-R(H)]/R(H)$, where $R(H)$ and $R(0)$ are the resistances with and without, respectively, a magnetic field of 5 T.

Figure 10 displays the same $R(T)$ dependencies with and without an applied magnetic field of 5 T for the thin ($d \simeq 70$ nm) (1) LSMO/LAO and (2) LSMO/BTO, and thick ($d \simeq 160$ nm) (3) LSMO/BTO and (4) LSMO/LAO films. Inset (a) shows the temperature dependence of the MR value for these films. Because the LSMO manganite did not undergo a real MI transition near T_C and manifests only a change in the slope of the $R(T)$ dependence, the MI temperatures were obtained from the analysis of the first derivative of $R(T)$, which is represented by the inset (b). It is seen that, for thick LSMO/BTO and LSMO/LAO, $T_P \simeq 275$ and 250 K, while, for the thin ones, $T_P \simeq 260$ and 220 K, respectively (denoted by arrows). Some magnetotransport characteristics of the investigated films are summarized in Table II.

V. DISCUSSION

Let us analyze the obtained results on the basis of the Millis model.[13] For a weak lattice strain ϵ and a cubic symmetry T_C can be expressed as

$$T_C(\epsilon) = T_{C0}\left(1 - \alpha\epsilon_B - \frac{1}{2}\Delta\epsilon_{JT}^2\right),$$

where $T_{C0}=T_C(\epsilon=0)$, $\alpha=(1/T_{C0})(dT_C/d\epsilon_B)$, and $\Delta =(1/T_{C0})(d^2T_C/d\epsilon_{JT}^2)$. The magnitudes of α and Δ represent

TABLE II. Magnetotransport characteristics for the investigated films.

Samples	Curie point T_C (K)	Coercive field H_c (Oe)	Saturation field H_s (Oe)	Remanence M_r/M_s (%)	Maximum magnetoresistance MR (%)[a]	MI transition T_P (K)
LCMO/BTO	250	100	3000	61	550 (17)	230
LCMO/LAO	230	300	6000	59	760 (9)	195
LSMO/BTO	310	100	800	73	80 (65)	275
LSMO/LAO	296	100	4000	31	50 (43)	250
LSMO/STO	315	100	1200	70	40 (38)	280

[a]In parentheses are the MR values at 300 K.

the relative weights for the symmetry-conserving bulk strain ϵ_B and the symmetry-breaking Jahn-Teller strain ϵ_{JT}, respectively. According to the model,[13] $\alpha \simeq 10$ for a reasonable electron-phonon coupling ($0.5 \leqslant \lambda \leqslant 1$) in these compounds, where λ is the electron-phonon-interaction constant, and $\Delta \simeq 5000$. Taking into account the fact that T_C for the strain-free bulk $La_{0.7}Ca_{0.3}MnO_3$ compound is $T_{C0} \simeq 265$ K (Ref. 36) and using the obtained values of ϵ_B, ϵ_{JT}, and T_C, we estimated Δ as 3000 and 1500 for LCMO/BTO and LCMO/LAO, and 7000, 5000, and 800 for LSMO/BTO, LSMO/LAO, and LSMO/STO, respectively. T_{C0} of 375 K was used for the strain-free bulk $La_{0.7}Sr_{0.3}MnO_3$ compound.[29] Those values, firstly, greatly differ from the model prediction (except the LSMO/LAO film) and, secondly, are strain dependent, which is impossible to treat in the framework of this model. A similar strong discrepancy between the model and the experiment was recently observed for the LCMO films deposited on STO and $NdGaO_3$.[14,15] The most plausible explanation for this disagreement is based on the existence of a dead layer or a parasitic phase located at the film/substrate interface, which leads to an additional influence on T_C together with lattice strain.[14,15,37] However, the cross-sectional HREM images did not manifest the appearance of any intensive defects close to the interface in the investigated films, and the temperature-dependent magnetization curves were testifying only the existence of a single-phase magnetic state. We argue that the following reasons lead to the observed discrepancy. First, it is connected with the relatively random selection of the bulk lattice parameters for the estimation of the in-plane and the out-of-plane strains, owing to strong variations between the experimental data found in the literature.[20,28–32,36,38–40] Second, even the annealed strain-free films have a different unit-cell volume from that of the bulk materials.[37,39] Therefore, we are sure that the correct testing of the Millis model[13] for the CMR films must be carried out by using the lattice parameters of annealed films as a "bulk," rather than the real bulk materials.

On the other hand, the elastic stress intensity in these films can be identified with the tetragonal distortion of the lattice. Table I shows that the tetragonal ratios are larger for the LCMO than those for the LSMO films. This can be explained by the different growth mechanism in these films. The HREM data reveal that LCMO demonstrates the epitaxial mode with an almost coherent interface between the substrate and the film, while the growth of LSMO is accompanied by dislocation formation, resulting in a semicoherent interface.

Let us consider in detail the influence of the lattice-strained state and the microstructure features on magnetotransport properties of the investigated films. Figure 7 shows that LCMO/BTO with a biaxial tensile in-plane lattice strain undergoes the magnetic transition at a higher temperature than that observed in LCMO/LAO with a biaxial compressive strain. It is well known that the electron-transfer integral in CMR materials is determined mainly by Mn-O bond length and Mn-O-Mn angle.[41] The final result for T_C can be approximately written as $T_C \sim \cos \varphi / d_{Mn-O}^{3.5}$, where φ is the tilt angle in the plane of the bond, and d_{Mn-O} is the Mn-O bond length.[42,43] It is reasonable to assume that the tetragonal elastic deformation of a crystal lattice, provided by compressive and tensile strains, results in the simultaneous change of the Mn-O bond length and the Mn-O-Mn angle, owing to the distorted vertex sharing of MnO_6 octahedra.[44] Taking into account the fact that the biaxial tensile in-plane lattice strain increases the Mn-O bond length, it would be reasonable to expect a significant reduction instead of the observed increase in T_C. Therefore, one can conclude that the variation of the Mn-O-Mn bond angle, controlled by lattice strain, plays a more important role for the spin ordering in CMR films than the attendant modification of the Mn-O bond length.

Table II shows that the LCMO/BTO film has a smaller saturation field and a larger remanent magnetization than the LCMO/LAO one. This is due to the magnetic anisotropy of strained epitaxial films, which is strongly correlated with the nature of the substrate-induced lattice-strain state. It is well known that the easy axis of the magnetization is always parallel to the direction of a tensile strain.[5,8] Consequently, in the LCMO/BTO film, an in-plane biaxial magnetic anisotropy is observed, while the easy axis is perpendicular to the LCMO/LAO film plane. The observed increase of the coercive field for LCMO/LAO can be connected with the column-like texture of the film,[30–32] which can play a role of additional pinning centers for magnetic domain walls during a magnetization reversal.

The LSMO films also demonstrate the influence of the substrate-induced lattice strain state on the magnetic properties, however, this effect is less manifested than for the LCMO ones. Similar to LCMO, the LSMO/BTO and the LSMO/STO films with biaxial tensile in-plane lattice strain demonstrate a higher T_C than the LSMO/LAO. This implies that in the LSMO films the ferromagnetic ordering is also governed by the tilt bond angle rather than the Mn-O bond length.

The relatively small value of the saturation field and the high remanence field testify that the LSMO films, in contrast to LSMO/LAO, deposited on BTO and STO have the in-plane easy axis, which is also coincident with data for the LCMO films. On the other hand, the coercive field remains the same for all films and does not depend on the substrate material. Therefore, the prepared LSMO films do not have large-size microstructural faults [for example, such as columnlike texture in LCMO/LAO (Refs. 30–32)] that can pin the magnetic domains during the magnetization reversal.

Figures 7 and 8 show that the difference between ZFC and FC magnetization curves at low temperature essentially depends on the substrate material. This phenomenon is usually treated as an existence of intrinsically inhomogeneous magnetic (or "cluster" glass) state governed by the electronic phase separation in the CMR materials.[35] The degree of magnetic inhomogeneity in the films can be expressed by $\Delta M^{FC}_{ZFC} = 100\% \times [M^{FC}(T) - M^{ZFC}(T)]/M^{FC}(T)$, where $M^{FC}(T)$ and $M^{ZFC}(T)$ are FC and the ZFC magnetization at a certain temperature. The ΔM^{FC}_{ZFC} values turn out to be significantly different for investigated films: 93, 74, 37, 20, and 0 % for LCMO/LAO, LCMO/BTO, LSMO/LAO, LSMO/BTO, and LCMO/STO, respectively. The higher degree of magnetic inhomogeneity is observed in the LCMO films with a larger tetragonal distortion of crystal lattice (see Table I) and a columnar microstructure,[30–32,45] which is formed through the biaxial in-plane strain accommodated during deposition. In contrast, the LSMO films demonstrate smaller tetragonal distortion due to the introduction of misfit dislocations during their growth, resulting in a more regular microstructure and a smaller degree of magnetic inhomogeneity. Therefore, this kind of magnetic inhomogeneity, which is connected with the observed difference in the FC and ZFC $M(T)$ dependences, has a crystallographic rather than an electronic nature, and is controlled by the lattice distortion and the microstructure defects.

The temperature dependencies of resistance represented by Figs. 9 and 10 are typical for the CMR films. For example, the MI transition temperature, which is determined at the peak of the $R(T)$ curve [for the LSMO films it is the peak of the first derivative $dR(T)/dT$ curve], is strongly correlated with T_C and can be expressed by a simple empirical relation in our case: $T_P \simeq 0.92T_C - 11.6$ K. On the other hand, the usual increase of MR value with the decreasing MI transition temperature is observed only for the LCMO films. Insets (a) and (b) in Fig. 10 display that the LSMO/BTO films demonstrate larger MR values compared to the LSMO/LAO ones, even though their MI transition temperatures are higher.

Thus, MR=80 and 110%, and $T_P \simeq 275$ and 260 K for LSMO/BTO with $d \simeq 160$ and 70 nm, respectively, while MR=50 and 91%, and $T_P \simeq 250$ and 220 K for LSMO/LAO with $d \simeq 160$ and 70 nm, respectively. The deposition of the LSMO film on the BTO layer leads to an increase in magnetoresistance. Moreover, the LSMO/BTO bilayered film demonstrates the maximal MR value at room temperature of about 65%.

VI. CONCLUSIONS

We have performed magnetotransport measurements on LCMO/BTO and LSMO/BTO bilayered films deposited by rf-magnetron sputtering using the "soft" (or powder) targets. For comparison, LCMO/LAO, LSMO/LAO, and LSMO/STO films have also been prepared. The HREM analysis reveals (i) the BTO layer has a tetragonal structure with the *c* axis normal to the film plane, (ii) LCMO/BTO and LSMO/BTO have the biaxial tensile in-plane and compressive out-of-plane strains, while LCMO/LAO and LSMO/LAO are exposed reversely to compressive in-plane and tensile out-of-plane strains, and (iii) LCMO has a coherent interface between the substrate and the film, while LSMO has a semi-coherent one, owing to the accumulation of misfit dislocations during the deposition.

It was shown that the films with a biaxial tensile in-plane lattice strain underwent the magnetic transition at a higher temperature than those with biaxial compressive ones. This implies that the variation of Mn-O-Mn bond angle, controlled by the lattice strain, plays a more important role in the formation of spin ordering in the CMR film than the modification in Mn-O bond length.

The LCMO/BTO, LSMO/BTO, the LSMO/STO films manifest an in-plane magnetic anisotropy, while the easy axis of magnetization is out-of-plane for the LCMO/LAO the LSMO/LAO systems. It was understood that the magnetic inhomogeneity, connected with the observed difference between FC and ZFC $M(T)$ dependences, is controlled by the lattice distortion and the microstructural defects. The obtained enhancement of magnetoresistance for the LSMO/BTO bilayered film at room temperature provides a significant contribution to the development of new hybrid ferromagnetic/ferroelectric devices.

ACKNOWLEDGMENTS

*Electronic mail: yplee@hanyang.ac.kr

[1] J. Volger, Physica (Utrecht) **20**, 49 (1954).

[2] R. von Helmolt, J. Wecker, B. Holzapfel, L. Schultz, and K. Samwer, Phys. Rev. Lett. **71**, 2331 (1993).

[3] S. Jin, T. H. Tiefel, M. McCormack, R. A. Fastnacht, R. Ramesh, and L. H. Chen, Science **264**, 413 (1994).

[4] R. A. Rao, D. Lavric, T. K. Nath, C. B. Eom, L. Wu, and F. Tsui, Appl. Phys. Lett. **73**, 3294 (1998).

[5] T. K. Nath, R. A. Rao, D. Lavric, C. B. Eom, L. Wu, and F. Tsui, Appl. Phys. Lett. **74**, 1615 (1999).

[6] J. R. Sun, C. F. Yeung, K. Zhou, L. Z. Zhou, C. H. Leung, H. K. Wong, and B. G. Shen, Appl. Phys. Lett. **76**, 1164 (2000).

[7] H. S. Wang, E. Wertz, Y. F. Hu, and Q. Li, J. Appl. Phys. **87**, 7409 (2000).

[8] R. Desfeux, S. Bailleul, A. Da Costa, W. Prellier, and M. Haghiri-Gosnet, Appl. Phys. Lett. **78**, 3681 (2001).

[9] A. Biswas, M. Rajeswari, R. C. Srivastava, T. Venkatesan, R. L. Green, Q. Lu, A. L. de Lozanne, and A. J. Millis, Phys. Rev. B **63**, 184424 (2001).

[10] S. Jacob, T. Roch, F. S. Razavi, G. M. Gross, and H.-U. Habermeier, J. Appl. Phys. **91**, 2232 (2002).

[11] M. Paranjape, A. K. Raychauhuri, N. M. Mathur, and M. G. Blamire, Phys. Rev. B **67**, 214415 (2003).

[12] Y. P. Lee, S. Y. Park, V. G. Prokhorov, V. A. Komashko, and V. L. Svetchnikov, Appl. Phys. Lett. **84**, 777 (2004).

[13] A. J. Millis, T. Darling, and A. Migliori, J. Appl. Phys. **83**, 1588 (1998).

[14] M. Bibes, L. Balcells, S. Valencia, J. Fontcuberta, M. Wojcik, E. Jedryka, and S. Nadolski, Phys. Rev. Lett. **87**, 067210 (2001).

[15] M. Bibes, S. Valencia, L. Balcells, B. Martínez, J. Fontcuberta, M. Wojcik, S. Nadolski, and E. Jedryka, Phys. Rev. B **66**, 134416 (2002).

[16] V. G. Prokhorov, V. A. Komashko, V. L. Svetchnikov, Y. P. Lee, and J. S. Park, Phys. Rev. B **69**, 014403 (2004).

[17] K. M. Satyalakshmi, S. S. Manoharan, M. S. Hegde, V. Prasad, and S. V. Subramanyam, J. Appl. Phys. **78**, 6861 (1995).

[18] W. Zhang, W. Boyd, M. Elliot, and W. Herrenden-Harkerand, Appl. Phys. Lett. **69**, 3929 (1996).

[19] J.-M. Liu and C. K. Ong, Appl. Phys. Lett. **73**, 1047 (1998).

[20] R. Mahendiran, S. K. Tiwary, A. K. Raychaudhuri, and T. V. Ramakrishnan, Phys. Rev. B **53**, 3348 (1996).

[21] J. Li, C. K. Ong, J.-M. Liu, Q. Huang, and S. J. Wang, Appl. Phys. Lett. **76**, 1051 (2000).

[22] V. G. Prokhorov, G. G. Kaminsky, V. A. Komashko, Y. P. Lee, J. S. Park, and H. C. Ri, Appl. Phys. Lett. **80**, 2707 (2002).

[23] G. Srinivasan, E. T. Rasmussen, B. J. Levin, and R. Hayes, Phys. Rev. B **65**, 134402 (2002).

[24] V. G. Prokhorov, G. G. Kaminsky, V. A. Komashko, J. S. Park, and Y. P. Lee, J. Appl. Phys. **90**, 1055 (2001).

[25] F. Jona and G. Shirane, *Ferroelectric Crystals* (Pergamon, New York, 1962), p. 108.

[26] R. Maier and J. L. Cohn, J. Appl. Phys. **92**, 5429 (2002).

[27] E. Snoeck, B. Warot, H. Ardhuin, A. Rocher, M. J. Casanove, R. Kilaas, and M. J. Hÿtch, Thin Solid Films **319**, 157 (1998).

[28] Q. Huang, A. Santoro, J. W. Lynn, R. W. Erwin, J. A. Borchers, J. L. Peng, K. Ghosh, and R. L. Greene, Phys. Rev. B **58**, 2684 (1998).

[29] M. C. Martin, G. Shirane, Y. Endoh, K. Hirota, Y. Moritomo, and Y. Tokura, Phys. Rev. B **53**, 14285 (1996).

[30] O. I. Lebedev, G. Van Tendeloo, S. Amelinckx, B. Leibold, and H.-U. Harbermeier, Philos. Mag. A **79**, 1561 (1999).

[31] O. I. Lebedev, G. Van Tendeloo, S. Amelinckx, H. L. Ju, and K. M. Krishnan, Philos. Mag. A **80**, 673 (2000).

[32] G. Van Tendeloo, O. I. Lebedev, and S. Amelinckx, J. Magn. Magn. Mater. **211**, 73 (2000).

[33] T. Walter, K. Dörr, K.-H. Müller, D. Eckert, K. Nenkov, M. Hecker, M. Lehmann, and L. Schultz, J. Magn. Magn. Mater. **222**, 175 (2000).

[34] F. Tsui, M. C. Smoak, T. K. Nath, and C. B. Eom, Appl. Phys. Lett. **76**, 2421 (2000).

[35] For a review, see E. Dagotto, T. Hotta, and A. Moreo, Phys. Rep. **344**, 1 (2001).

[36] Y. H. Li, K. A. Thomas, P. S. I. P. N. de Silva, L. F. Cohen, A. Goyal, M. Rajeswari, N. D. Mathur, M. G. Blamire, J. E. Evetts, T. Venkatesan, and J. L. MacManus-Driscoll, J. Mater. Res. **13**, 2161 (1998).

[37] J. Z. Sun, D. W. Abraham, R. A. Rao, and C. B. Eom, Appl. Phys. Lett. **74**, 3017 (1999).

[38] J. Blasko, J. Gareia, J. M. DeTeresa, M. R. Ibarra, P. A. Algarabel, and C. Marquina, J. Phys.: Condens. Matter **8**, 7427 (1996).

[39] J. Hayakawa, H. Asano, M. Matsui, and H. Takahashi, J. Magn. Magn. Mater. **84**, 84 (2000).

[40] M. Zeise, H. C. Semmelhack, and P. Busch, J. Magn. Magn. Mater. **246**, 327 (2002).

[41] H. Y. Hwang, S. W. Cheong, N. P. Ong, and B. Batlogg, Phys. Rev. Lett. **77**, 2041 (1996).

[42] C. M. Varma, Phys. Rev. B **54**, 7328 (1996).

[43] M. Medarde, M. Mesot, P. Lacorre, S. Rosenkranz, P. Fisher, and K. Grobcht, Phys. Rev. B **52**, 9248 (1995).

[44] Y. Tokura, Y. Tomioka, H. Kuwahara, A. Asamitsu, Y. Moritomo, and M. Kasai, J. Appl. Phys. **79**, 5288 (1996).

[45] H.-U. Harbermeier, Physica B **321**, 9 (2002).